Switching-Sequence Control of a Higher Order Power-Electronic System Driving a Pulsating Load

Debanjan Chatterjee, *Student Member, IEEE*, and Sudip Kumar Mazumder, *Fellow, IEEE*

***Abstract*—In a conventional linear-control design of a higher order power-electronic system (PES), the gains of the control laws are typically determined by small-signal analysis of the averaged model of the PES. The closed-loop control of such a PES (driving a pulsating load that periodically shifts the equilibrium) using its small-signal model is often found to be unsatisfactory with regard to the overall stability and performance. To address the challenges in control design for a PES driving such a nonlinear time-varying pulsating load, this paper delineates an optimal switching-sequence-based control (SBC) scheme, which applies stability-bound switching sequence(s) to the PES. A novel method has been formulated to ensure the reachability of the PES dynamics based on its switching sequence in terms of the time horizon of the switching sequence and the allocation of this time among the switching states of the same switching sequence. This is ascertained by modeling the PES and the pulsating load as a nonlinear map and then using this map and multiple Lyapunov functions determined by solving a set of linear-matrix inequalities corresponding to each of the switching states of a given switching sequence. It has been further shown that the knowledge of the stability bounds of a reachable switching sequence helps in reducing the online computation time for optimal SBC associated with solving the optimization problem by reducing the overall search space. Finally, to validate the optimal SBC, an experimental GaN-FET-based 100-kHz Ćuk-PES has been fabricated and tested on a pulsating load. The overall SBC is implemented on a low-cost TMS320F28335 DSP, which also implements an observer to preclude the need for plurality of sensors for the higher order Ćuk-PES. The overall performance of the SBC is found to be satisfactory under varied dynamical conditions.**

***Index Terms*—Control, estimator, GaN FET, Lyapunov, map, nonlinear, online, optimal, pulsating load, switching sequence.**

I. Introduction

HIGHER order power-electronic systems (PESs) that supply nonlinear pulsating loads with higher temporal scales [1], [2] require careful attention in control design since large-signal variations in voltages and currents may lead to stability and power-quality issues. For such a PES, typical linear controllers (that are designed to operate in the vicinity of the system equilibrium) as well as several nonlinear controllers are often unable to ensure large-signal stability and satisfactory performance. Fig. 1 illustrates the performance of one such recently outlined nonlinear control law [3] for a Ćuk PES feeding a 1 kHz pulsating load (the pulsating frequency is so chosen, such that resonance due to the presence of poles and zeros of the PES in the vicinity of 5 kHz are not excited). The control law failed to regulate the output voltage of the PES at such higher temporal scales as shown in Fig. 1. This is primarily because the gains of the nonlinear controller synthesized using a reduced-order slow-scale model of the PES are pushed to the limits causing instability. This implies that, for such a pulsating-load application, control strategy that uses model of PES encompassing wider temporal scales is needed so that satisfactory large-signal stability of the PES is ensured while exhibiting fast dynamic response.

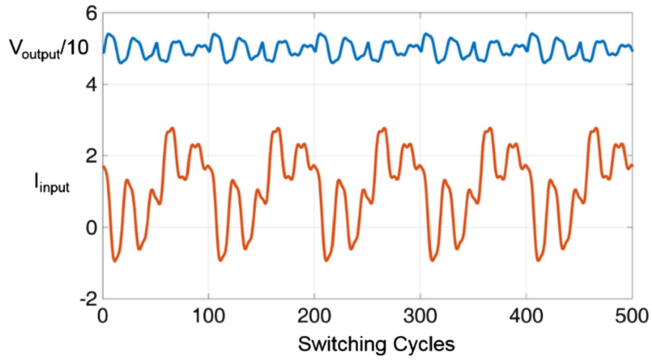

Fig. 1. Illustration of the PES response using a nonlinear controller [3] feeding a pulsating load with a repetition rate of 1 kHz. The upper and lower traces show instabilities in the scaled output voltage and the input inductor current, respectively. The results are for a Ćuk PES described in Section IV. The figure highlights inability of the controller to give desired performance.

Advanced sliding-mode controllers [4], [5] may yield robust closed-loop PES feeding such nonlinear time-varying pulsating loads. Notwithstanding, for a higher order PES, efforts leading to computation of the explicit control action based on a Lyapunov function is non-trivial. Backstepping- and passivity-based control laws [6], [7] use smooth averaged models for control formulation that mitigate the range of temporal scales. Dynamic feedback linearization [8] may be a possibility as well; however,

Manuscript received October 20, 2018; revised January 4, 2019 and March 17, 2019; accepted April 26, 2019. Date of publication May 8, 2019; date of current version October 18, 2019. This work was supported in part by the U.S. Office of Naval Research under Award N00014-17-1-2695 and in part by the U.S. Department of Energy's Office of Energy Efficiency and Renewable Energy (EERE) under Solar Technologies Office (SETO) Agreement No. EE0008349. Recommended for publication by Associate Editor T. Suntio. *(Corresponding author: Sudip Kumar Mazumder.)*

The authors are with the Department of Electrical and Computer Engineering, University of Illinois at Chicago, Chicago, IL 60607-7101 USA (e-mail: dchatt4@uic.edu; mazumder@uic.edu).

Color versions of one or more of the figures in this paper are available online at http://ieeexplore.ieee.org.

Digital Object Identifier 10.1109/TPEL.2019.2915830

See http://www.ieee.org/publications_standards/publications/rights/index.html for more information.

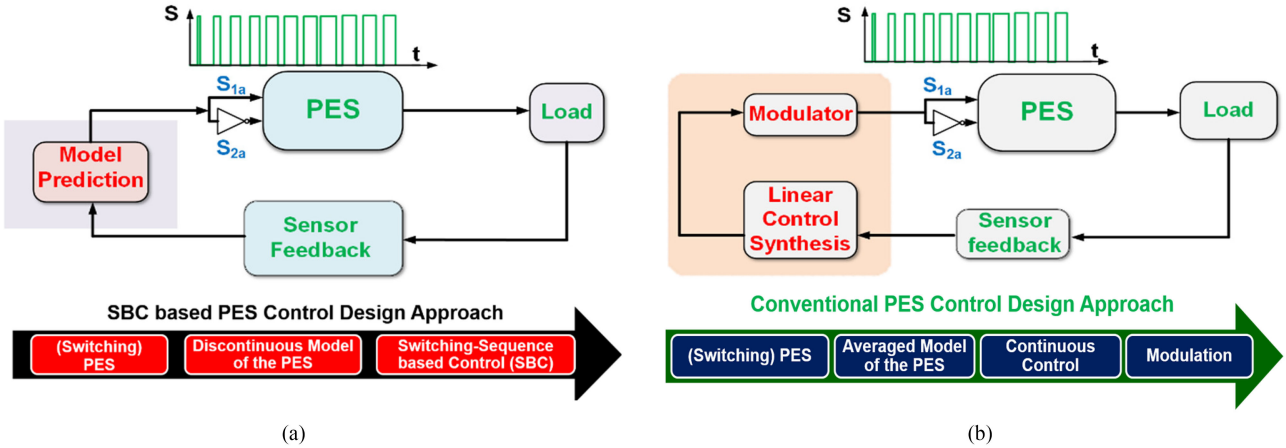

Fig. 2. Illustration of (a) SBC scheme for PES and (b) a conventional linear control scheme. SBC precludes the need for a PWM modulator.

for a higher order non-minimum phase PES driving a nonlinear pulsating load determining the convergence of the zeroth-order dynamics is challenging.

Optimal controllers, based on multiscale discontinuous models of the PES, demonstrate promise. In that regard, model-predictive-control (MPC) laws solve the underlying optimal-control problems by controlling the switching states of a PES. As a result, the resulting switching sequence in an MPC when applied to a PES may result in satisfactory performance but the stability of the PES is not always guaranteed [9]. This becomes an issue of importance for PES supplying a pulsating load exhibiting wide and fast temporal scales. In contrast, optimal switching-sequence-based control (SBC) achieves optimality by directly controlling the stability-bound switching sequence(s) that yields robust performance of the PES even when it is driving a fast-switching pulsating load. Fig. 2 delineates the distinction between a conventional linear-control modulator, as illustrated in [10] and [11].

The work in [12]–[18] outlines how the modern optimal controllers, that underlie SBC, have evolved as attractive solutions for controlling PES that go beyond simple regulation to superior spectral shaping and switching-loss mitigation [12]. The work in [11], [19] focuses on optimization techniques for high-frequency PESs so that the optimal solutions can be obtained online.

Optimal controllers for lower order non-minimum phase PES have been previously discussed in [15]–[19]; however, they do not take into consideration nonlinear loads for a higher order PES operating at high frequency. The work in [20]–[22] primarily show deteriorated PES behavior with nonlinear reduced damped loads and the challenges in control formulation. However, for pulsating loads, most of the existing literatures delineate hardware modifications of PESs in terms of increased energy storage. The work in [28] delineates topological advances required in a PES structure to power nonlinear pulsating loads, and the work in [29] further adds on how to reduce pulsating load impacts on microgrids. The work in [30] uses coupled magnetics to improve PES dynamic response for pulsating loads. Similarly, the work in [31] depicts modulation technique for a PES powering a pulsating load. In [1], aircraft generating systems supplying pulsating loads and their design guidelines, in terms of topology and control, have been outlined. The work in [32] describes high-power pulsating-load applications, where large magnetics have been used for energy storage to deliver power to the load. Such systems operate at low pulse-repetition frequencies as reiterated in [33]. Similarly, the work in [2] uses compensating devices for intermittent energy storage to improve PES dynamic response. The work in [34] also talks about using enhanced storage devices and simpler control techniques to supply pulsating load applications. Using minimal storage capabilities, the work in [35] presents a neural-network (NN)-based control framework to address problems related to pulsating loads in shipboards, but such systems operate at low switching frequencies which make the use of NN techniques feasible. Also, the work in [36] delineates advanced controllers to mitigate the effects of pulsed power loads, but the prediction models used are linearized about operating points and implemented in high-end processors that does not encompass online time savings in low-end digital processors.

This paper delineates an optimal SBC approach to mitigate the challenges associated with control design of a higher order non-minimum-phase isolated Ćuk PES supplying a higher frequency pulsating load. The optimal SBC directly maneuvers the duration of switching states in a switching sequence of the Ćuk PES through minimization of an appropriate cost-function. A novel methodology to analyze the reachability of the PES dynamics in terms of the time horizon of a switching sequence has also been provided. The approach delineated in this manuscript may benefit solution of problems related to (but not limited to) electromagnetic launch systems [37], motor-drives with pulsating current loads [38], and design of controllers for linear induction motors [39] having pulsating current levels that can be used in launch systems.

Overall, SBC involves three broad steps. Section II outlines the first step regarding the discrete modeling of the PES feeding the pulsating load. Subsequently, Section III provides the method for reachability analysis of the PES in terms of its switching sequence. In the final step, outlined in Section IV, optimization of the PES using one or more of these reachable

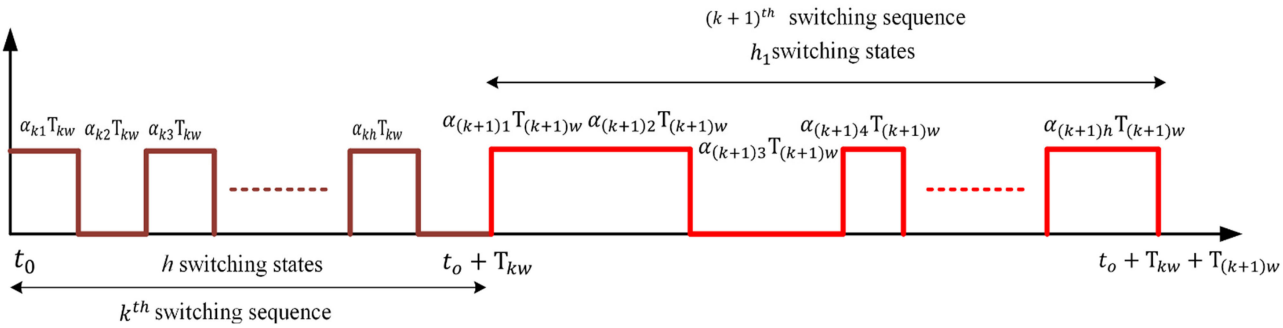

Fig. 3. Illustration of the kth and $(k+1)$th switching sequence of a PES comprising h and h_1 switching states, respectively.

switching sequence(s) to ensure desired performance optimality. This section also provides the generalized framework for SBC architecture for a PES. Subsequently, Section IV-A delineates the online optimal SBC synthesis for a specific Ćuk PES, which includes the description of the discrete prediction model of the PES, the performance index for the control, and the observer design that precludes full-sensor-feedback requirement for the higher order PES. The results have been discussed in Section V, while conclusions have been drawn in Section VI.

II. Modeling of the PES Driving a Pulsating Load

SBC is a closed-loop optimal policy, where given a kth switching sequence with switching states, its time horizon (T_{kw}) and the allocation $(\alpha_{k1}, \ldots, \alpha_{kh})$ of this time among each of its switching states are computed on the fly. Fig. 3 portrays two such switching sequences of a PES, to explain the point, having time horizon T_{kw} and $T_{(k+1)w}$, respectively, along with the time allocation $[(\alpha_{k1}, \ldots, \alpha_{kh})$ for the first sequence and $(\alpha_{k+1_1}, \ldots, \alpha_{k+1_{h1}})$ for the second sequence] amongst the switching states (h switching states in the first switching sequence and h_1 switching states in the second switching sequence). The optimal values of these sets of parameters in SBC are determined in two steps. Initially, the outer limits of these two sets of parameters are determined using a Lyapunov-based reachability analysis. This is detailed in Section III, which requires a hybrid nonlinear model of the PES driving the pulsating load. Subsequently, the optimal values of these two sets of parameters from the above set are determined in real time by solving an optimization problem outlined in Section IV. In this section, the nonlinear model of the PES driving a pulsating load is outlined.

Fig. 4 depicts a pulsating load with the dynamics defined by the following harmonic series:

$$i_{\text{load}}(t) = \frac{1}{2} i_{\text{load1}} + \sum_{m=1}^{\infty} \{a_m \cos(w_m t) + b_m \sin(w_m t)\} \tag{1a}$$

$$\frac{1}{2} i_{\text{load1}} = \text{average}\left(i_{\text{load}}(t)\right) \tag{1b}$$

$$a_m = \frac{\sin(2m\pi D_{\text{load}})}{m\pi} \Delta i_{\text{load}} \tag{1c}$$

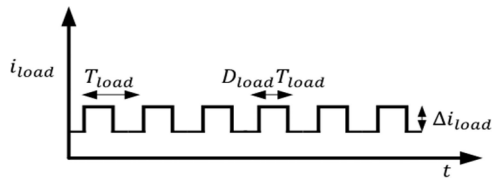

Fig. 4. Illustration of a pulsating load with transition level denoted by Δi_{load}, duty cycle denoted by D_{load}, and the switching time period of the pulse denoted by T_{load}.

$$b_m = \frac{1 - \cos(2m\pi D_{\text{load}})}{m\pi} \Delta i_{\text{load}}. \tag{1d}$$

The physical meaning of the symbols in (1a) are depicted in Fig. 4, where D_{load} denotes the duty cycle of the pulsating load, Δi_{load} denotes the magnitude of the load transition, and T_{load} denotes the time period of the load pulse. Inverse of T_{load} gives the pulsating load frequency f_{load}.

For a practical pulsating load with finite slew rate

$$\dot{\hat{x}}(t) = \hat{A}_{kn}\hat{x}(t) + \hat{B}_{kn} + \frac{1}{2} i_{\text{load1}} + + \sum_{m=1}^{\infty} \{a_m \cos(w_m t) + b_m \sin(w_m t)\} \tag{2}$$

where $\hat{A}_{kn}$ and $\hat{B}_{kn}$ are matrices that describe the PES without the pulsating load and have been defined in [3]. Equation (2) is rewritten in a compressed form as follows:

$$\dot{x}(t) = A_{kn} x(t) + B_{kn} \tag{3}$$

where A_{kn} and B_n are functions of the pulsating-load dynamics and defined in the Appendix for a particular PES.

Next, (3) is translated to error coordinates using $e(t) = x(t) - x^*$, where $e(t)$ represents the error vector, while x^* represents the steady-state values of the PES states. In the error coordinate, (3) is modified as follows:

$$\dot{e}(t) = A_{kn} e(t) + \overline{B_{kn}} \tag{4}$$

where $\overline{B_{kn}} = -(B_{kn} + A_{kn}x^*)$. Discretizing (4), one obtains the following expression for the jth discrete sample

$$e(j+1) = A_{knd} e(j) + B_{knd} \tag{5}$$

where

$$A_{knd} = \prod_{n=1}^{2h} \exp^{A_{kn} T_{kw} \alpha_{k(2h-n+1)}} \tag{6a}$$

$$\begin{aligned} B_{knd} = & \left(\prod_{n\neq 1}^{2h} \exp^{A_{k(2h-n+1)} T_{kw} \alpha_{k(i)}} \right) \\ & \times \left(\exp^{A_{k1} T_{kw} \alpha_{k1}} - I \right) A_{k1}^{-1} \overline{B_{k1}} \\ & + \left(\prod_{n\neq 1,2}^{2h} \exp^{A_{k(2h-n+1)} T_{kw} \alpha_{k(i)}} \right) \\ & \times \left(\exp^{A_{k2} T_{kw} \alpha_{k2}} - I \right) A_{k2}^{-1} \overline{B_{k2}} + \cdots \\ & + \left(\exp^{A_{k2h} T_{kw} \alpha_{k2h}} - I \right) A_{k2h}^{-1} \overline{B_{k2h}}. \end{aligned} \tag{6b}$$

III. PES Stability Analysis

The work in [9] delineates the theory behind computation of the reachability analysis of a switching sequences of a PES. However, the theory does not explicitly consider the time horizon of the switching sequence. The reachability analysis that is laid forth, apart from creating a set of reachable switching sequences for the PES, helps in determining the range of the time allocation of the nth switching state in the kth switching sequence (i.e., α_{kn}) and the length of time horizon of the kth switching sequence (i.e., T_{kw}) that aids in real-time execution of SBC. For the kth switching sequence illustrated in Fig. 3, with h switching states satisfying $0 \leq \alpha_{kn} \leq 1$, $\sum_{n=1}^{h} \alpha_{kn} = 1$, and $P_{kn} = P_{kn}^T$ being positive-definite matrices, a piecewise-discrete (multiple) Lyapunov function $V_k(j) = \sum_{n=1}^{h} e(j)^T P_{kn} e(j)$ is used to obtain the gradient of the multiple Lyapunov function

$$\begin{aligned} \nabla V_k(e) &= V_k(j+1) - V_k(j) \\ &= \sum_{n=1}^{h} \alpha_{kn} \left(e(j+1)^T P_{kn} e(j+1) \right. \\ &\quad \left. - e(j)^T P_{kn} e(j) \right). \end{aligned} \tag{7}$$

$$\begin{aligned} \nabla V_k(e) = & \sum_{n=1}^{h} \alpha_{kn} \begin{pmatrix} e(j) \\ 1 \end{pmatrix}^T \\ & \times \begin{bmatrix} (A_{knd}^T P_{kn} A_{knd} - P_{kn}) & A_{knd}^T P_{kn} B_{knd} \\ B_{knd}^T P_{kn} A_{knd} & B_{knd}^T P_{kn} B_{knd} \end{bmatrix} \\ & \times \begin{pmatrix} e(j) \\ 1 \end{pmatrix}. \end{aligned} \tag{8}$$

According to the Lyapunov-method of stability analysis for a discrete system, the PES state trajectories converge to (i.e., reach) an orbit if $\nabla V_k(e) < 0$ which results in the following

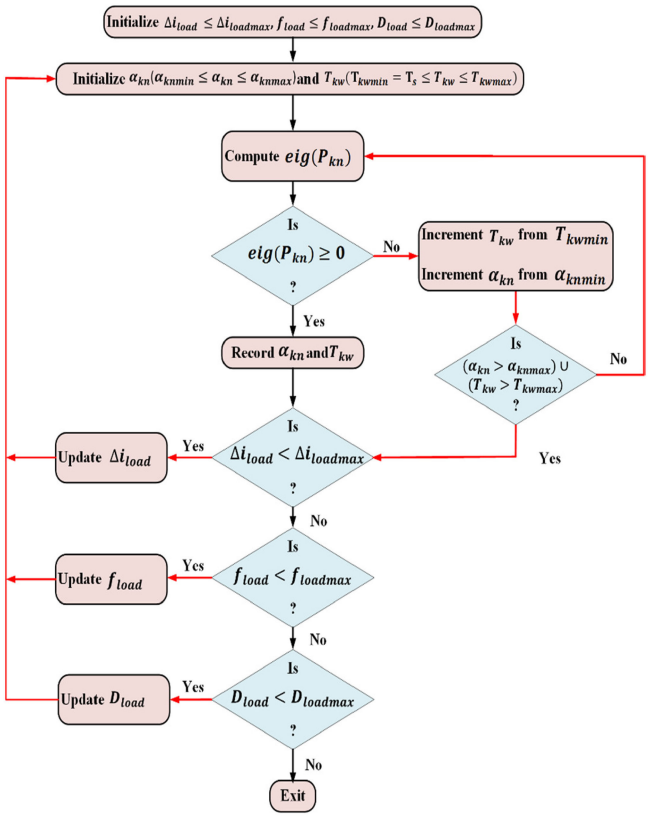

Fig. 5. Flowchart of PES stability analysis methodology.

linear matrix inequality (LMI):

$$\sum_{n=1}^{h} \alpha_{kn} \begin{bmatrix} (A_{knd}^T P_{kn} A_{knd} - P_{kn}) & A_{knd}^T P_{kn} B_{knd} \\ B_{knd}^T P_{kn} A_{knd} & B_{knd}^T P_{kn} B_{knd} \end{bmatrix} < 0 \tag{9}$$

which is formulated as a feasibility problem and solved using the LMI tool in MATLAB. The flowchart shown in Fig. 5 delineates how the LMIs are solved to get α_{kn} and T_{kw} that ensure PES reachability (i.e., orbital existence) given a range of pulsating load dynamics. To ensure periodic orbital stability, the range of T_{kw} should always include $T_{kw\min} = T_s$, where T_s denotes the switching frequency of the PES. The bounds on Δi_{load}, f_{load}, and D_{load}, denoted by $\Delta i_{\text{loadmax}}$, f_{loadmax}, and D_{loadmax}, respectively, come directly from hardware limitations which will be discussed in Section V.

IV. SBC Scheme

Fig. 6 delineates the entire SBC scheme for a PES. The steps incurred in the SBC synthesis are delineated as follows.

1) Initially, depending on the PES topology and its switching behavior, a set of feasible switching sequences for the PES is determined following [9].
2) Subsequently, a comprehensive discontinuous dynamical model of the PES and the pulsating load is developed, as outlined in Section II.

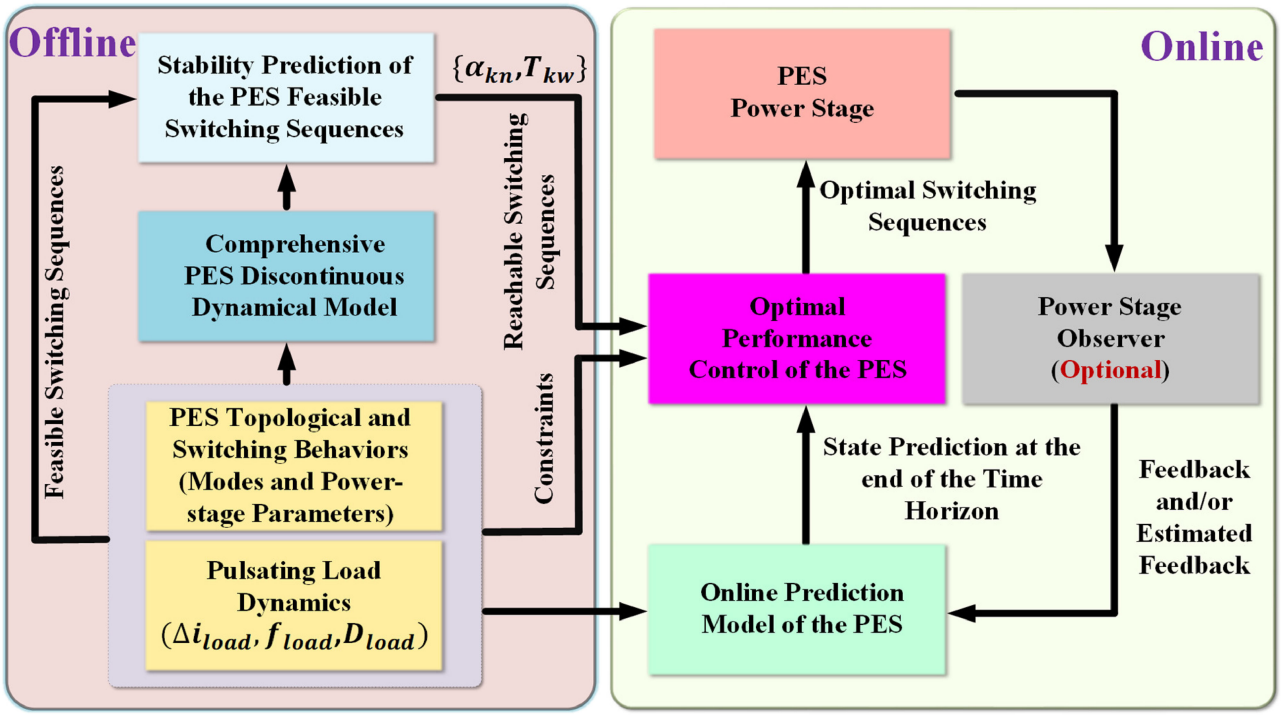

Fig. 6. Illustration of the SBC scheme for the PES driving a pulsating load.

3) Subsequently, using the feasible switching sequences in "1," the model in "2," the PES parameters and the pulsating-load parameters (i.e., $\Delta i_{\text{load}}, f_{\text{load}}, D_{\text{load}}$), a subset of reachable switching sequences (that ensure the convergence of the PES dynamics) is determined offline using the stability-analysis methodology outlined in Section III. The goal of this analysis is to determine the bounds on α_{kn} and T_{kw} for the reachable switching sequences that are used for the online execution of SBC for optimally controlling the performance of the PES.

Subsequently, for fast real-time execution of the SBC, an online prediction model of the PES is synthesized that closely matches the dynamics of the model in "2." The prediction model is synthesized using a discrete map of the PES, which is obtained by patching together the individual maps corresponding to each switching state. If the PES has h switching states in a reachable switching sequence, the prediction model can be synthesized as in (10), where $\hat{A}_{knd}$ and $\hat{B}_{knd}$ have been defined in (11a) and (11b)

$$\hat{x}(j+1) = \hat{A}_{knd}\hat{x}(j) + \hat{B}_{knd} \tag{10}$$

$$\hat{A}_{knd} = \prod_{n=1}^{2h} \exp^{\hat{A}_{kn} T_{kw} \alpha_{k(2h-n+1)}} \tag{11a}$$

$$\hat{B}_{knd} = \left[\left(\prod_{n\neq 1}^{2h} \exp^{\hat{A}_{k(2h-n+1)} T_{kw} \alpha_{k(n)}} \right) \times \left(\exp^{\hat{A}_{k1} T_{kw} \alpha_{k1}} - I \right) \hat{A}_{k1}^{-1} \hat{B}_{k1} + \left(\prod_{n\neq 1,2}^{2h} \exp^{\hat{A}_{k(2h-n+1)} T_{kw} \alpha_{k(n)}} \right) \times \left(exp^{\hat{A}_{k2} T_{kw} \alpha_{k2}} - I \right) \hat{A}_{k2}^{-1} \hat{B}_{k2} + \cdots + \left(\exp^{\hat{A}_{k2h} T_{kw} \alpha_{k2h}} - I \right) \hat{A}_{k2h}^{-1} \hat{B}_{k2h}. \right. \tag{11b}$$

4) Next, a cost function, denoted by $C(\alpha_{kn}, T_{kw})$ is formulated and an online optimal control problem is solved online to perform online performance control of the PES. The online optimization problem can be summarized as to determine α_{kn} and T_{kw} that minimizes the following cost function:

$$C(\alpha_{kn}, T_{kw}) = (\hat{x}^* - \hat{x}(j+1))^T P (\hat{x}^* - \hat{x}(j+1)) \tag{12}$$

given the constraints on PES states and bounds on α_{kn} and T_{kw}. In (12), P is a positive-definite matrix that provides scaling of the terms in the cost function. As shown in Fig. 6, the optimization problem yields reachable switching sequences with optimal values of α_{kn} and T_{kw} (i.e., $\alpha_{kn_{\text{opt}}}, T_{kw_{\text{opt}}}$) that are fed to the PES power stage.

5) Finally, and if full-state feedback is not possible to preclude the need for large number of sensors in a higher order PES, a closed-loop state observer is synthesized

as follows:

$$\overline{\hat{x}}\,(j+1) = \overline{\hat{A}_{knd}}\overline{\hat{x}}\,(j) + \overline{\hat{B}_{knd}} \tag{13}$$

$$\overline{\hat{A}_{knd}} = \prod_{n=1}^{2h} \exp^{\hat{A}_{kn}T_{kw}(\alpha_{k(2h-n+1)}+\Delta(\alpha_{k(2h-n+1)}))} \tag{14a}$$

$$\begin{aligned}\overline{\hat{B}_{knd}} = &\left(\prod_{n\neq 1}^{2h} \exp^{\hat{A}_{k(2h-n+1)}T_{kw}(\alpha_{k(n)}+\Delta\alpha_{k(n)})}\right)\\ &\times\left(\exp^{\hat{A}_{k1}T_{kw}(\alpha_{k1}+\Delta\alpha_{k1})} - I\right)\hat{A}_{k1}^{-1}\hat{B}_{k1}\\ &\times\left(\prod_{n\neq 1,2}^{2h} \exp^{\hat{A}_{k(2h-n+1)}T_{kw}(\alpha_{k(n)}+\Delta\alpha_{k(n)})}\right)\\ &\times\left(\exp^{\hat{A}_{k2}T_{kw}(\alpha_{k2}+\Delta\alpha_{k2})} - I\right)\hat{A}_{k2}^{-1}\hat{B}_{k2} + \cdots\\ &+\left(\exp^{\hat{A}_{k2h}T_{kw}(\alpha_{k2h}+\Delta\alpha_{k2h})} - I\right)\hat{A}_{k2h}^{-1}\hat{B}_{k2h}.\end{aligned} \tag{14b}$$

where the correction terms, denoted by Δ, have been discussed for a PES in Section IV-A. Fig. 7 shows a flowchart as used for the implementation of SBC online. To be precise, the algorithm minimizes, for a given set of reachable switching sequences, the cost function$C(\alpha_{kn}, T_{kw})$ with respect to α_{kn} and T_{kw}. For $T_{kw} > T_{kw\min}$, both α_{kn} and T_{kw} are optimized which ensures convergence of the PES dynamics from an initial condition to an orbit [9] using reachable switching sequence(s). Whenever $T_{kw} \leq T_{kw\min}$, we consider $T_{kw} = T_{kw\min} = T_s$ and only α_{kn} has to be optimized, which ensures convergence to the periodic orbit [9] or steady state.

A. Case Illustration: Synthesizing SBC for a Ćuk DC/DC PES (Ćuk-PES) Following Sections II–IV

To realize the SBC scheme online, a GaN-FET-based 100-kHz Ćuk-PES is fabricated and tested. The online SBC scheme for the Ćuk-PES, as shown inFig. 8, which constitutes of an online prediction model synthesis, followed by cost function formulation and lastly, the observer design, is discussed below.

1) Prediction Model: The higher order isolated Ćuk-PES operates in the continuous-conduction-mode (CCM) of operation. The modes of operation have been shown in the Appendix to ease comprehension. For the fundamental switching sequence of the Ćuk-PES, if A_{k1} and B_{k1} and A_{k2} and B_{k2} are matrices in successive switching states having time allocations of α_{k1} and α_{k2}, respectively, and T_{kw} be the time horizon of the fundamental switching sequence, then by stacking together the following equations:

$$\hat{x}\,(j') = e^{A_{k1}\alpha_{k1}T_{kw}}\hat{x}\,(j) + \left(e^{A_{k1}\alpha_{k1}T_{kw}} - I\right)A_{k1}^{-1}B_{k1} \tag{15}$$

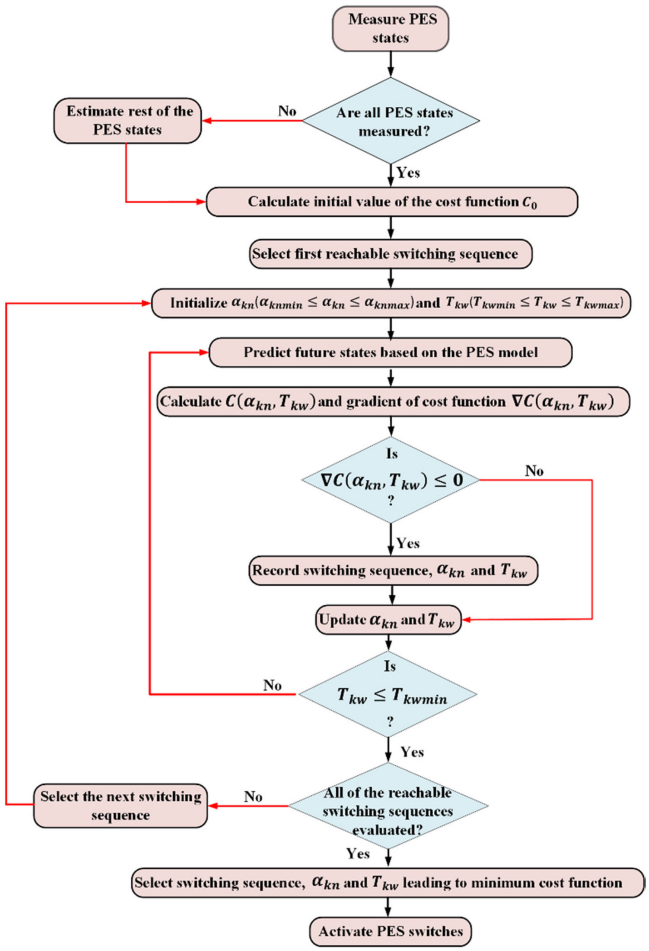

Fig. 7. Flowchart for online implementation of the SBC.

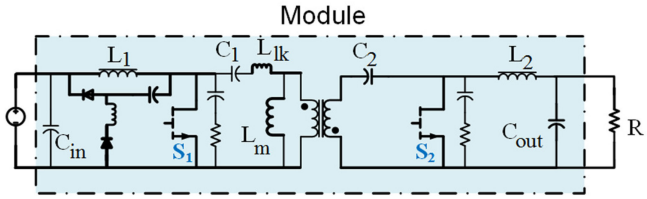

Fig. 8. Schematic of the Ćuk PES with GaN-FET-based switches S_1 and S_2.

$$\hat{x}\,(j+1) = e^{A_{k2}\alpha_{k2}T_{kw}}\hat{x}\,(j') + \left(e^{A_{k2}\alpha_{k2}T_{kw}} - I\right)A_{k2}^{-1}B_{k2} \tag{16}$$

one obtains the following nonlinear map:

$$\begin{aligned}\hat{x}\,(j+1) = &\, e^{A_{k1}\alpha_{k1}T_{kw}+A_{k2}\alpha_{k2}T_{kw}}\hat{x}\,(j)\\ &+ e^{A_{k2}(\alpha_{k2})T_{kw}}\left(\left(e^{A_{k1}\alpha_{k1}T_{kw}} - I\right)A_{k1}{}^{-1}B_{k1}\right)\\ &+ \left(e^{A_{k2}\alpha_{k2}T_{kw}} - I\right)A_{k2}{}^{-1}B_{k2}\end{aligned} \tag{17}$$

where $\hat{x}(j')$ and $\hat{x}(j+1)$ denote the system states after time evolution $\alpha_{k1}T_{kw}$ and $\alpha_{k1}T_{kw} + \alpha_{k2}T_{kw}$, respectively, from initial value $\hat{x}(j)$. The system dynamics satisfy $\alpha_{k1} + \alpha_{k2} = 1$.

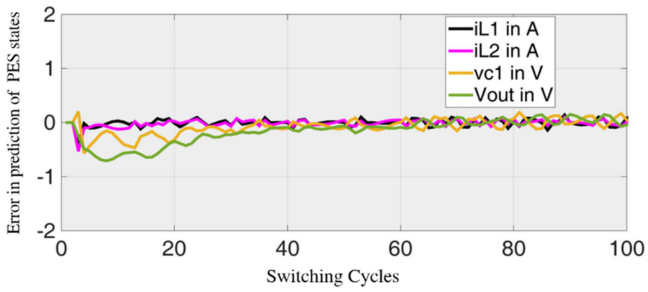

Fig. 9. Error in the prediction of the PES states based on the nonlinear Ćuk-PES model (18) and the approximated nonlinear model (19). The legends from top to bottom represent the input and output inductor currents, blocking capacitor and output voltage. The *y*-axis denotes both voltage and current (a value of 0.25 corresponds to both –0.25 V and 0.25 A).

The exponential terms in (17) is simplified using first-order Euler's approximation to form the following nonlinear prediction model:

$$\begin{aligned}\hat{x}\,(j+1) = {} & \left(I + A_{k1}\alpha_{k1}T_{kw} + A_{k2}\alpha_{k2}T_{kw}\right)\hat{x}\,(j) \\ & + \left(A_{k2}\alpha_{k2}T_{kw} + I\right)\left(\alpha_{k1}T_{kw}B_{k1}\right) \\ & + \alpha_{k2}T_{kw}B_{k2}. \end{aligned} \tag{18}$$

Given any set of initial conditions from the sensors/observers, this approximation is found to be viable for high sampling rates, as depicted in the first 100 switching cycles of the system in Fig. 9, sampled at 100 kHz. The first 50 switching cycles encompass system start-up and hence the approximation is viable for both start-up and steady-state. The schematic of the Ćuk-PES, as shown in Fig. 8, includes more passive elements including the magnetizing and leakage inductance of the transformer, which have not been incorporated in the prediction model for reasons described in the Appendix.

2) Cost Function: The generalized framework for the discrete cost function of the non-minimum phase Ćuk-PES as a current regulation problem has been outlined as follows:

$$\begin{aligned} C\left(\alpha_{k1}, T_{kw}\right) = {} & \delta_1 (1/IL_{\text{ref}})^2 * (IL_{\text{ref}} - iL_1\,(j))^2 \\ & + \gamma_1 * (\alpha_{k1}\,(j) - \alpha_{k1}\,(j-1))^2 \\ & + \gamma_2 * (T_{kw}\,(j) - T_{kw}\,(j-1))^2 \end{aligned} \tag{19a}$$

$$\begin{aligned} IL_{\text{ref}} = {} & G_p\left(V_{\text{ref}} - V_{\text{out}}\,(j)\right) \\ & + G_I \sum_j \left(V_{\text{ref}} - V_{\text{out}}\,(j)\right) T_{kw} + I_{ff} \end{aligned} \tag{19b}$$

where IL_{ref} and V_{ref} are the references for the input inductor current $iL_1(j)$, and the output voltage $V_{\text{out}}(j)$, both defined at the jth discrete sample. The last two terms in $C(\alpha_{k1}, T_{kw})$ help in mitigation of control input chattering between two successive discrete samples. The terms G_p and G_I, along with the feedforward term I_{ff}, help in mitigation of steady-state error quickly. The cost function has been designed based on the principles mentioned in [4], [21], [40], and [41]. The terms δ_1, γ_1, and γ_2 effectively maneuver the control bandwidth and transient response, and their tuning process has been discussed in [32] and [42].

3) Observer Design: SBC when implemented on a higher order PES may necessitate a state observer to reduce the cost associated with full-state feedback. A state observer for the Ćuk-PES is created using (17). Notwithstanding, the actual system dynamics may not precisely match the prediction of model (17) due to the parasitic, transformer nonlinearity, and switching dead time. Hence, a correction mechanism is needed to ensure that the error between the observed and the actual system dynamics converges to zero. The equation of the observer is as follows:

$$\begin{aligned} \overline{\hat{x}}\,(j+1) = {} & e^{A_{k1}(\alpha_{k1}+\Delta\alpha_{k1})T_{kw} + A_{k2}(1-(\alpha_{k1}+\Delta\alpha_{k1}))T_{kw}}\,\overline{\hat{x}}\,(j) \\ & + e^{A_{k2}(1-(\alpha_{k1}+\Delta\alpha_{k1}))T_w} \\ & \times \left(\left(e^{A_{k1}(\alpha_{k1}+\Delta\alpha_{k1})T_{kw}} - I\right) {A_{k1}}^{-1} B_{k1}\right) \\ & + \left(e^{A_{k2}(1-(\alpha_{k1}+\Delta\alpha_{k1}))T_{kw}} - I\right) {A_{k2}}^{-1} B_{k2}. \end{aligned} \tag{20}$$

$\overline{\hat{x}}(j+1)$ denotes the observed system states after time evolution $T_{kw} + \Delta\alpha_{k1}T_{kw}$, where$\Delta\alpha_{k1} = K_p(V_{\text{out}}(j) - \overline{\widehat{x_4}}(j)) + K_I \sum_j (V_{\text{out}}(j) - \overline{\widehat{x_4}}(j))T_{kw}$, $V_{\text{out}}(j)$ is the sampled output voltage of the hardware Ćuk-PES at the jth discrete instant, and $\overline{x_4}(j)$ is the output voltage of the observer at the same time instant. The observer takes $V_{\text{out}}(j)$ and $V_{\text{in}}(j)$ as the inputs and K_p and K_I are proportional and integral gains. Parameters α_{k1} and T_{kw} are varied across the operating range and the values of the closed-loop gains are computed taking into consideration large-signal stability of the observer.

V. Results

The section has been organized as follows. The hardware setup, along with the higher order Ćuk-PES experimental prototype, as shown in Fig. 10(a) and (b), is discussed first. Next, the analytical-stability results for the system and how it helped in SBC execution online have been delineated with experimental results.

The SBC algorithm is implemented on a TMS320F28335 digital signal processor (DSP) using code composer studio version 3.3, and the switching sequence, with the allocated switching states (α_{k1} and α_{k2}) and time horizon (T_{kw}), is used to drive the GS66508B GaN-FET-based Ćuk-PES operating at switching frequency ($f_s = 1/T_s$) of 100 kHz. The power-stage parameters used are provided in Table I. The detailed hardware design has been discussed in [43]. The dc electronic load 6050A from HP has been used to emulate the pulsating load, while hall current sensor TCP312A (30 A) with TCPA300 amplifiers (both two) from Tektronix have been used for current measurements. Agilent 6030A dc power supply has been used as regulated input power supply for the PES, while a bench power supply from Tenma has been used as control supply. Isolated four-channel oscilloscope TPS 2024B from Tektronix has been used to capture experimental results for the PES.

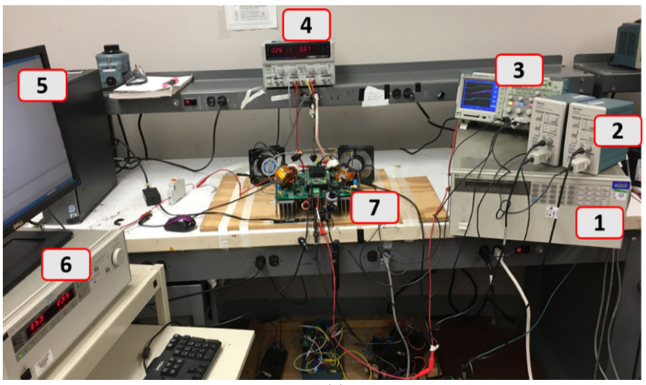

(a)

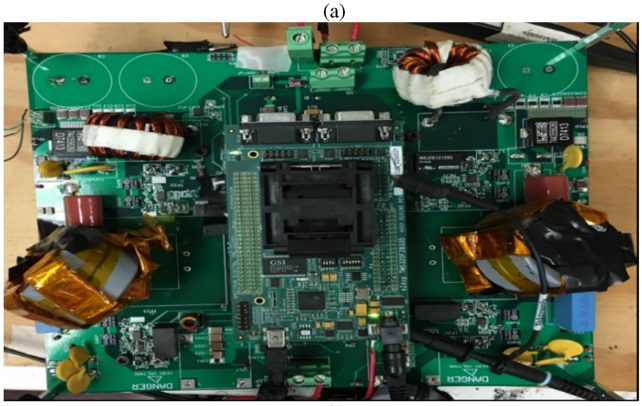

(b)

Fig. 10. (a) Entire experimental platform has been shown. The components are (1) dc electronic load, (2) current sensor, (3) oscilloscope, (4) the control supply, (5) the PC running code composer studio version 3.3, (6) the input dc power supply, and (7) the experimental hardware PES. (b) The PCB realization (top view) of the GaN-FET-based Ćuk-PES.

TABLE I
POWER-STAGE-PARAMETERS FOR THE ĆUK-PES

Input voltage range (V_{in})	Output voltage range (V_{out})	Input inductance (L_1)	Output inductance (L_2)	Input capacitance (C_{in})
0-50 V	0-170 V	50 μH	100 μH	4.4 μF
Output capacitance (C_{out})	Input blocking capacitance (C_1)	Output blocking capacitance (C_2)	Switching frequency ($1/T_s$)	Transformer turns ratio (N)
5 μF	6.8 μF	1.5 μF	100 kHz	2

Load-transition level (Δi_{load}) of up to 5 A and load duty cycle $(D_{\text{load}})$of up to 90% is considered as they can be realized in the Ćuk-PES hardware prototype. The Bode plot of the open-loop transfer function from α_{k1} to V_{out} is shown in Fig. 11; it shows resonant poles and zeros of the higher order Ćuk-PES located below 5 kHz. As such, to avoid the excitation of system resonance, an upper limit of f_{load} is considered to be well below 5 kHz. Since f_{load} of 2 kHz can be safely realized in hardware prototype, the reachability analysis derived in Section III is restricted to$\Delta i_{\text{load}} \leq$ 5 A, $f_{\text{load}} \leq$ 2 kHz, and $D_{\text{load}} \leq$ 90%.

The importance of the stability-criterion in the form of LMI is twofold. Considering the fundamental switching sequence of the

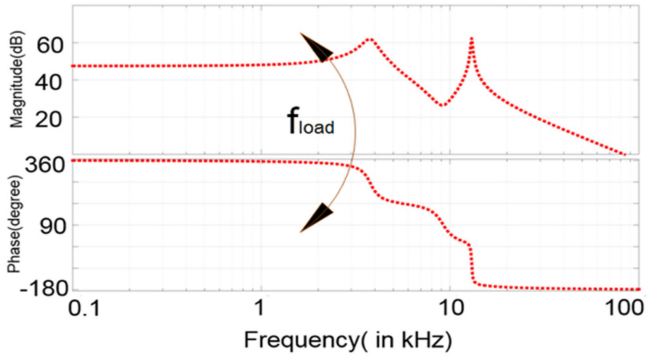

Fig. 11. Illustration of open-loop Bode plot of $\hat{V}_{\text{out}}/\hat{\alpha}_{k1}$ of the Ćuk-PES, where f_{load} denotes the pulsating load frequency, where $\hat{V}_{\text{out}}$ and $\hat{\alpha}_{k1}$ are the perturbed small-signal variables.

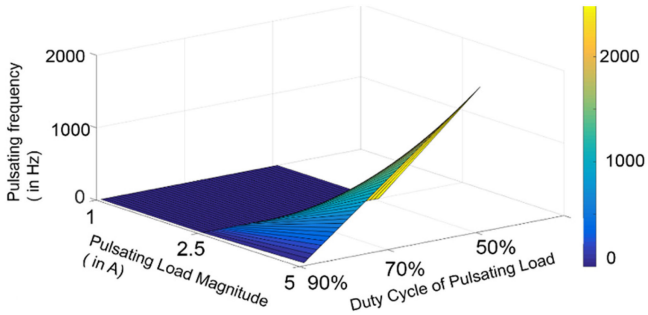

Fig. 12. Region of reachable operation of the PES.

Ćuk-PES (with α_{k1} and α_{k2} representing the time allocation of switching states in the sequence, T_{kw} as the time horizon of the switching sequence and given the constraint $\alpha_{k1} + \alpha_{k2} = 1$), the analysis aids in the following:

1) Investigation of the impacts of $\Delta i_{\text{load}} \leq$ 5 A, $f_{\text{load}} \leq$ 2 kHz, and $D_{\text{load}} \leq$ 90% on the reachability of the system dynamics;
2) Determination of the allowable ranges of α_{k1} and T_{kw} that stabilize the Ćuk-PES across $\Delta i_{\text{load}} \leq$ 5 A, $f_{\text{load}} \leq$ 2 kHz, and $D_{\text{load}} \leq$ 90%.

All analytical results are for $V_{\text{in}} = 30$ V and $V_{\text{out}} = 50$ V. Using the aforementioned values of pulsating-load dynamics in the LMIs defined by (9), reachable ranges of α_{k1} and T_{kw} are computed for $\Delta i_{\text{load}} \leq$ 5 A, $f_{\text{load}} \leq$ 2 kHz, and $D_{\text{load}} \leq 90\%$ that are used for real-time execution of SBC.

The impacts of load variations on the reaching conditions of the Ćuk-PES are investigated by solving (9). The region on the contour in Fig. 12 represents operating conditions that ensure reachability of the system dynamics. The region of reachability denotes that there existsα_{k1} and $T_{kw}$with variation of D_{load}, Δi_{load}, and f_{load} for which system dynamics can be stabilized. Fig. 12 shows that for the Ćuk-PES, while the region of reachable operation does not change with pulsating load magnitudes lower than $\Delta i_{\text{load}} = 2.5$ A for lower pulsating frequencies, for $\Delta i_{\text{load}} > 2.5$ A at higher pulsating frequencies, the region of reachable operation keeps on diminishing. As such,

progressively reduced pulsating duty cycles are attainable and further beyond $\Delta i_{\text{load}} = 4$ A, $f_{\text{load}} = 2$ kHz, and $D_{\text{load}} = 65\%$, there exists no α_{k1} and T_{kw} that can make the system dynamics reachable.

The aforementioned theoretical analysis precludes control law formulation. However, to investigate whether the experimental results match the theoretical predictions, an SBC law, due to its fast-transient response and seamless control formulation has been used and operation within and outside the reachability contour are investigated. For validation of operation within the reachable contour, Fig. 13(a) shows the Ćuk-PES response for the operating condition $\Delta i_{\text{load}} = 1$ A, $f_{\text{load}} = 0.2$ kHz, and $D_{\text{load}} = 50\%$. The system exhibits stable response as the operating point defined by f_{load}, D_{load}, and Δi_{load} lie on the reachable region in Fig. 12.

Fig. 13(b) shows the Ćuk-PES response at $\Delta i_{\text{load}} = 1$ A, $f_{\text{load}} = 0.2$ kHz, and $D_{\text{load}} = 50\%$ when an electrolytic capacitor of 1 mF is placed at the input. At increased input capacitance, the pulsating input current (shown by the green trace) gets smoothed off, which leads to uncorrupted input dc supplies. Fig. 13(c) shows system response for the more stringent operating condition $\Delta i_{\text{load}} = 2.5$ A, $f_{\text{load}} = 1$ kHz, and $D_{\text{load}} = 90\%$, which lies on the boundary of the reachable region in Fig. 12 as well. Fig. 13(d) shows system response for the operating condition $\Delta i_{\text{load}} = 4$ A, $f_{\text{load}} = 2$ kHz, and $D_{\text{load}} = 65\%$ which also lies on the boundary of the reachable region.

Finally, for further validation of operation within the reachable contour, a case illustration has been demonstrated, where the load-step (Δi_{load}) and duty cycle (D_{load}) have been kept at the value imitating the worst-case scenario, and only the pulsating frequency has been gradually changed, and whether the proposed SBC could achieve satisfactory performance has been verified in Fig. 14. SBC provided satisfactory performance given the limited computational capabilities of the low-end microcontroller used for implementation.

For validation of operation outside the reachable contour, Fig. 15 shows the response of the Ćuk-PES for operating points that do not lie on the reachable contour in Fig. 12. Operating the system beyond the reachable region at $\Delta i_{\text{load}} = 5$ A, $f_{\text{load}} = 2$ kHz, and $D_{\text{load}} = 65\%$ yields an unstable system resulting in oscillatory currents and voltages. The oscillations eventually lead to distorted output voltage and currents in the unstable system. The onset of the oscillations has been highlighted in Fig. 15(a), where the Ćuk-PES is regulating its output voltage to 50 V before operation beyond the reachable regime. The analysis in Fig. 12 also shows that for $\Delta i_{\text{load}} = 1$ A, $f_{\text{load}} = 0.2$ kHz, and $D_{\text{load}} = 50\%$, operating the system for $T_{kw} > 20\,\mu$s results in instability. In Fig. 15(b), the Ćuk-PES is operated by setting $T_{kw} = 26\,\mu$s $(> 20\,\mu$s) which, as predicted, yields an unstable system.

Now that the region of reachable operation, as shown in Fig. 12, has been experimentally validated, we explore the following: if the Ćuk-PES has to operate at a certain Δi_{load}, f_{load}, and D_{load}, the ranges of α_{k1} and T_{kw} that would ensure the PES reachability at every Δi_{load}, f_{load}, and D_{load} can be determined. Fig. 16 shows the maximum allowable α_{k1} for the Ćuk-PES with

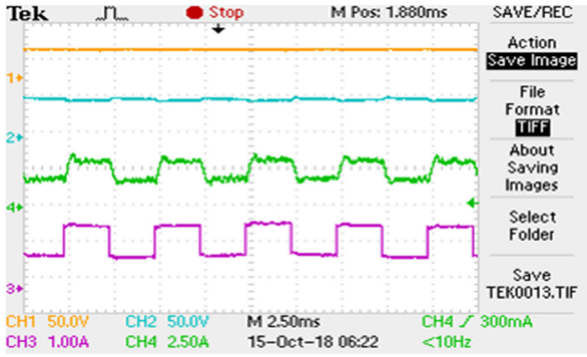

(a)

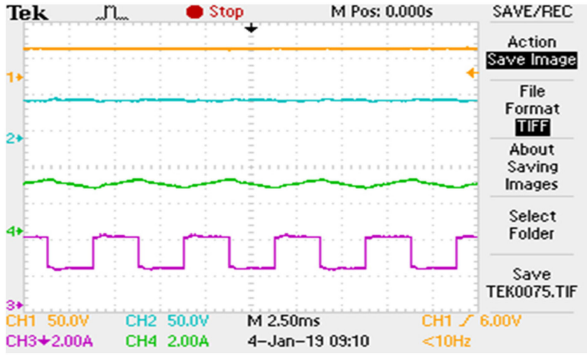

(b)

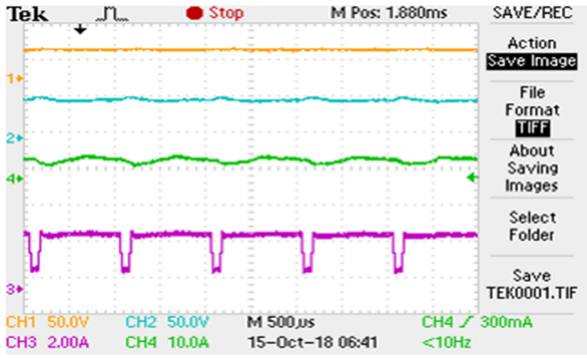

(c)

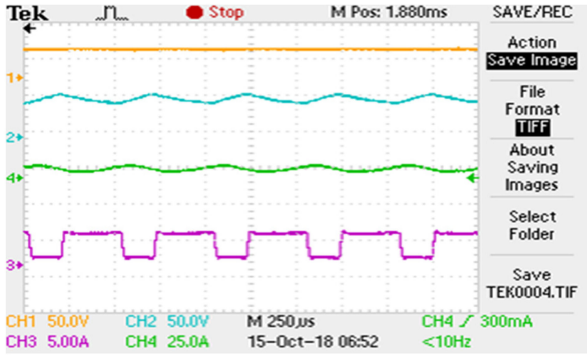

(d)

Fig. 13. In (a)–(d), the traces from top to bottom represent input and output voltages and input and output currents of the system. (a) Ćuk-PES response for $\Delta i_{\text{load}} = 1$ A, $f_{\text{load}} = 0.2$ kHz, and $D_{\text{load}} = 50\%$. (c) PES response for $\Delta i_{\text{load}} = 2.5$ A, $f_{\text{load}} = 1$ kHz, and $D_{\text{load}} = 90\%$, respectively. (d) Ćuk-PES response for $\Delta i_{\text{load}} = 4$ A, $f_{\text{load}} = 2$ kHz, and $D_{\text{load}} = 65\%$. (b) By increasing the input capacitance to 1 mF, the pulsation in the input ripple current in (a) (i.e., for $\Delta i_{\text{load}} = 1$ A, $f_{\text{load}} = 0.2$ kHz, and $D_{\text{load}} = 50\%$) is mitigated.

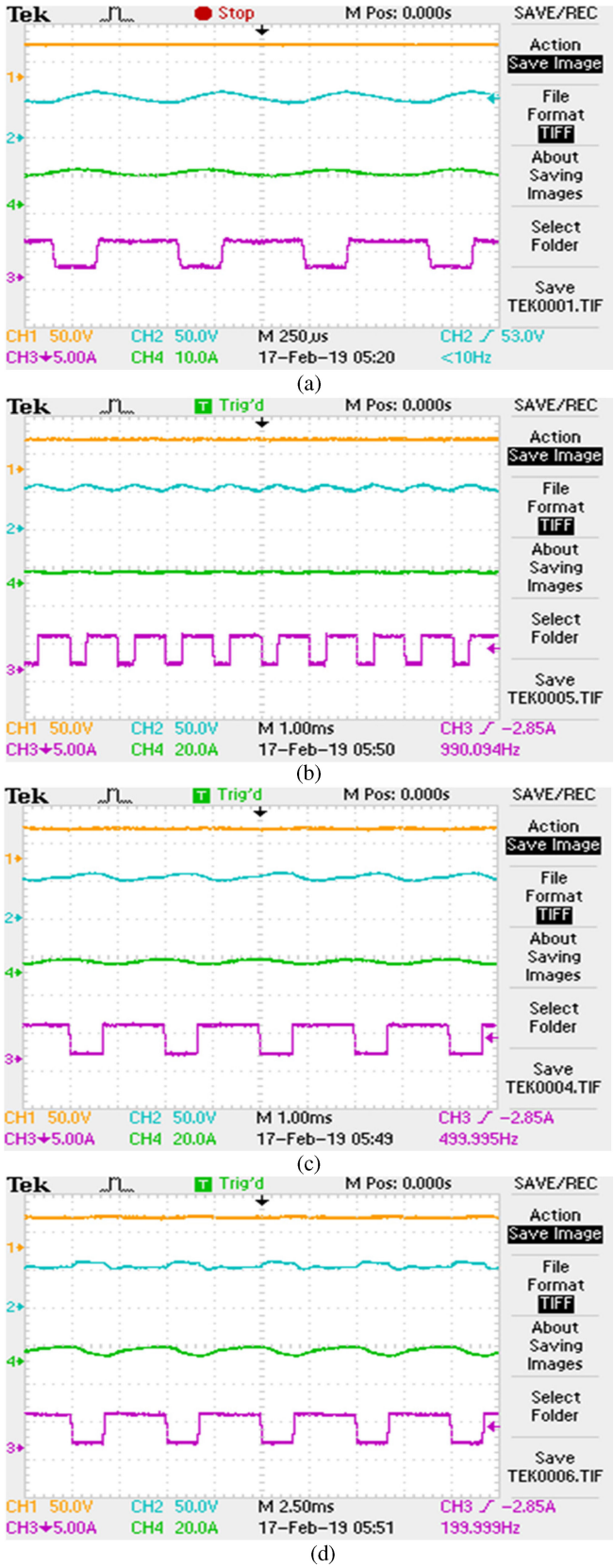

Fig. 14. In (a)–(d), the traces from top to bottom represent input and output voltages and input and output currents of the system. The Ćuk-PES response for $\Delta i_{\text{load}} = 4\,\text{A}$, $D_{\text{load}} = 65\%$ and (a) $f_{\text{load}} = 1.5\,\text{kHz}$, (b) $f_{\text{load}} = 1\,\text{kHz}$, (c) $f_{\text{load}} = 0.5\,\text{kHz}$, and (d) $f_{\text{load}} = 0.2\,\text{kHz}$. The pulsating load frequency has been changed from the worst-case load condition.

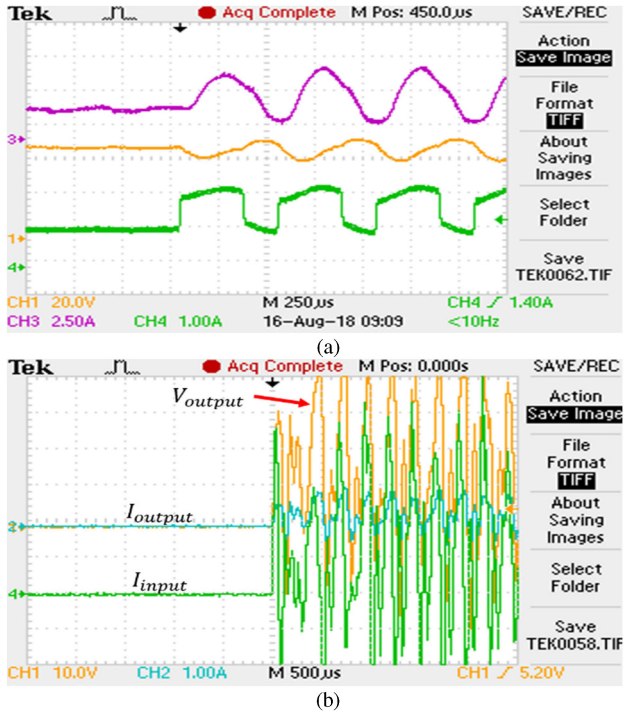

Fig. 15. (a) Ćuk-PES response for $\Delta i_{\text{load}} = 5\,\text{A}$, $f_{\text{load}} = 2\,\text{kHz}$, and $D_{\text{load}} = 65\%$ at the onset of instability. In (a) the traces from top to bottom represent input current, output voltage, and output current. (b) Unstable operation of the Ćuk-PES is captured for operation at $\Delta i_{\text{load}} = 1\,\text{A}$, $f_{\text{load}} = 0.2\,\text{kHz}$, and $D_{\text{load}} = 50\%$ at $T_{kw} = 26\,\mu\text{s}(> 20\,\mu\text{s})$. The traces from top to bottom represent output voltage, output current, and input current.

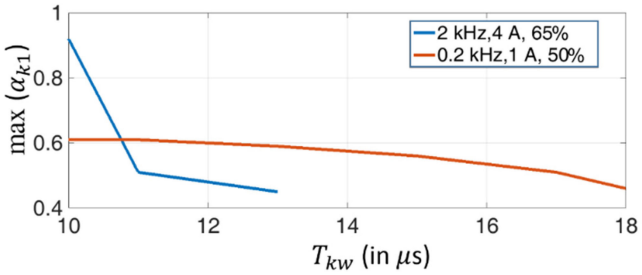

Fig. 16. Variations of α_{k1} with T_{kw} for $\Delta i_{\text{load}} = 1\,\text{A}$, $f_{\text{load}} = 0.2\,\text{kHz}$, and $D_{\text{load}} = 50\%$ and $\Delta i_{\text{load}} = 4\,\text{A}$, $f_{\text{load}} = 2\,\text{kHz}$, and $D_{\text{load}} = 65\%$.

respect to T_{kw}. Increasing the T_{kw} limits the maximum duty cycle available to ensure reachability. Fig. 16 shows the limits on α_{k1} and T_{kw} for extreme cases of the pulsating-load dynamics. Using this analysis, a bound on α_{k1} and T_{kw} is obtained for the PES operation. Operation beyond the limit of α_{k1} and T_{kw} obtained may lead to unstable PES behavior.

The bounds on α_{k1} (which also set the bounds for α_{k2}) and T_{kw} help in saving computation time for online execution in SBC, which enables implementation using low-cost hardware realizable without the need for sophisticated algorithms in the high-frequency Ćuk-PES. Fig. 16 shows that for loads with relatively slower scales of $\Delta i_{\text{load}} \leq 1\,\text{A}$, $f_{\text{load}} \leq 0.2\,\text{kHz}$, and $D_{\text{load}} \leq 50\%$, the maximum α_{k1} is capped at 0.61 and maximum T_{kw} is capped at 18 μs. Hence, any optimization algorithm to solve the online optimal SBC must look for values of

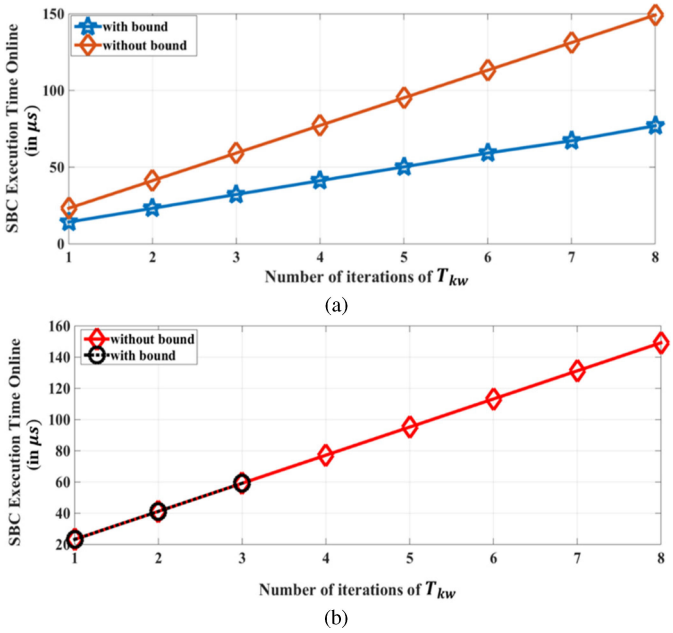

Fig. 17. (a) Experimentally obtained online SBC execution time, with and without offline reachability analysis for number of iterations of T_{kw} for loads below $\Delta i_{\text{load}} = 1\,\text{A}, f_{\text{load}} = 0.2\,\text{kHz}$, and $D_{\text{load}} = 50\%$. (b) Experimental comparative study of the online SBC execution time for $\Delta i_{\text{load}} = 4\,\text{A}$, $f_{\text{load}} = 2\,\text{kHz}$, and $D_{\text{load}} = 65\%$ as a function of number of iteration of T_{kw}.

$0 < \alpha_{k1} \leq 0.61$ and $T_{kw} \leq 18\,\mu\text{s}$. The minimum value of T_{kw} is dictated by the Ćuk-PES switching time T_s which is 10 μs leading to $10 \leq T_{kw} \leq 18\,\mu\text{s}$. For a simple brute-force search using resolution of α_{k1} to be 0.02, and T_{kw} to be 1 μs, Fig. 17(a) shows the saving in computation time for real-time execution of SBC.

For the Ćuk-PES operating at $\Delta i_{\text{load}} = 4\,\text{A}$, $f_{\text{load}} = 2\,\text{kHz}$, and $D_{\text{load}} = 65\%$, the maximum allowable time horizon is $T_{kw} \cong 13\,\mu\text{s}$ beyond which there exists no α_{k1} for which the system can reach an output voltage of 50 V for an input voltage of 30 V. Hence, for $\Delta i_{\text{load}} = 4\,\text{A}$, $f_{\text{load}} = 2\,\text{kHz}$, and $D_{\text{load}} = 65\%$, the online optimal SBC has to look for values of $0 < \alpha_{k1} \leq 0.9$ and $10 \leq T_{kw} \leq 13\,\mu\text{s}$, as shown in Fig. 16. Fig. 16, hence, shows that the blue trace which corresponds to $\Delta i_{\text{load}} = 4\,\text{A}$, $f_{\text{load}} = 2\,\text{kHz}$, and $D_{\text{load}} = 65\%$ stops at 13 μs which proves that no α_{k1} can provide reachability for $T_{kw} \geq 13\,\mu\text{s}$. Although the upper limit of α_{k1} has increased for this case, the range of T_{kw} has decreased, which saves online execution time for SBC. Hence, looking for admissible values of α_{k1} and T_{kw} yields a computation time of 59.2 μs, as shown in Fig. 17(b). If the bound on T_{kw} is not obtained, then the search time to execute the online SBC increases considerably.

Next, it is investigated whether online execution of the SBC by limiting the ranges of T_{kw} and α_{k1}, ascertained using the reachability analysis, deteriorates the performance of the Ćuk-PES. Fig. 18(a) and (b) show the Ćuk-PES performance variation at $\Delta i_{\text{load}} = 1\,\text{A}$, $f_{\text{load}} = 0.2\,\text{kHz}$, and $D_{\text{load}} = 50\%$, with and without bounds on α_{k1} and T_{kw}, respectively. Fig. 18(c) and (d) show the same PES performance variation at $\Delta i_{\text{load}} = 4\,\text{A}$, $f_{\text{load}} = 2\,\text{kHz}$, and $D_{\text{load}} = 65\%$, with and without bounds on

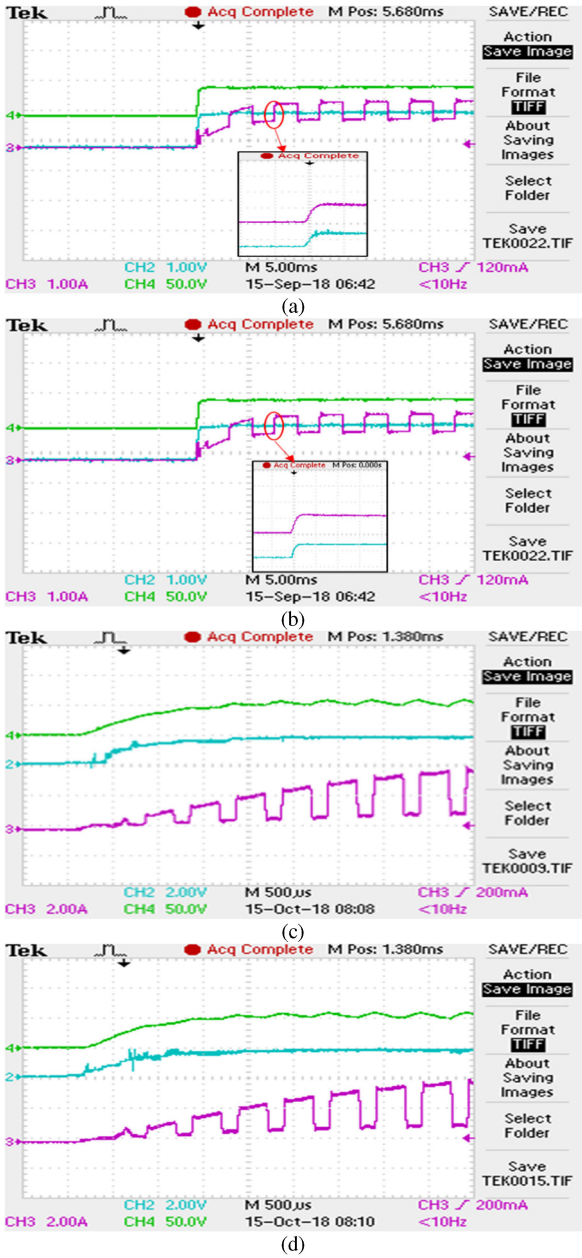

Fig. 18. (a) and (b) start-up response of the PES for $\Delta i_{\text{load}} = 1\,\text{A}$, $f_{\text{load}} = 0.2\,\text{kHz}$, and $D_{\text{load}} = 50\%$ without and with bounds on α_{k1} and T_{kw}, respectively. The horizontal scale is $500\,\mu\text{s/div}$ in the subplots in (a) and (b). (c) and (d) Ćuk-PES start-up response without and with bounds on α_{k1} and T_{kw}, respectively, for $\Delta i_{\text{load}} = 4\,\text{A}$, $f_{\text{load}} = 2\,\text{kHz}$, and $D_{\text{load}} = 65\%$. The channels 2, 3, and 4 represent α_{k1}, output current, and output voltage, respectively in (a)–(d).

α_{k1} and T_{kw}, respectively. The start-up response shows no significant deterioration of the Ćuk-PES performance in the two cases. Thus, the savings in the computation time of SBC is realized without tangible performance degradation at the prediction extremities.

Fig. 19(a) and (b) further validate the fact that computational time savings does not come at much reduced PES performance by plotting the convergence time of the output voltage to its steady-state value after the load-transition event has occurred

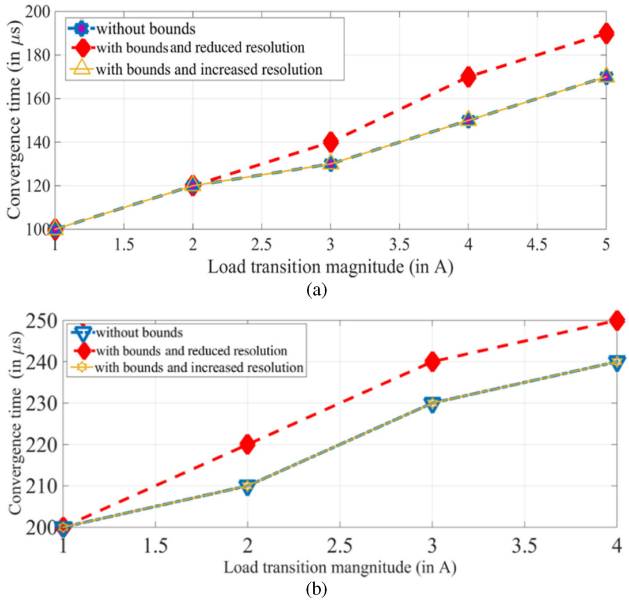

Fig. 19. (a) Comparative study of the experimental convergence time of the output voltage after load transition has occurred at $f_{\rm load} = 0.2\,$kHz and $D_{\rm load} = 50\%$ for gradually increasing load transition levels. (b) Comparative study of the experimental convergence time of the output voltage after load transition has occurred at $f_{\rm load} = 2\,$kHz and $D_{\rm load} = 65\%$ for gradually increasing load-transition levels.

for $f_{\rm load} = 0.2\,$kHz and $D_{\rm load} = 50\%$ and $f_{\rm load} = 2\,$kHz and $D_{\rm load} = 65\%$. At the extreme load conditions possible for the Ćuk PES of $f_{\rm load} = 2\,$kHz, $D_{\rm load} = 65\%$, and $\Delta i_{\rm load} = 4\,$A, there is delay of as low as $20\,\mu$s considering the high switching frequency of the PES. It is a tradeoff for implementing such computationally intensive control at low-end processors at high switching frequency. Due to limited computational capability of the low-cost industrial DSP used, the resolution of the control commands T_{kw} and α_{k1} has been fixed in the experiment to be $1\,\mu$s and 0.02, respectively. Hence, both the results with and without bounds have been obtained at fixed resolution. However, the resolution of the control inputs can be further increased along with modifications of the coefficients (γ_1 and γ_2) in the cost function, to bridge the gap in convergence times, as shown in the comparative study in Fig. 19.

VI. Conclusion

Control of a higher order PES driving a pulsating load using SBC, which solves an underlying optimal-control problem using pre-determined reachable switching sequences of the PES, has been delineated in this paper. Initially, using a nonlinear map of the PES, feeding a pulsating load, a discrete multiple-Lyapunov-function-based methodology to ascertain the reachability of the PES dynamics, in terms of its switching sequence and the time duration of the sequence and the allocation of that time among the switching states of the same sequence, is determined. Subsequently, an online optimal SBC formulation is outlined that uses these pre-determined limits on the reachable-switching-sequence duration and its distribution among the switching states of the same sequence. By doing so, the overall computation time for online SBC execution is expected to be reduced without affecting the overall control performance of the PES.

Subsequently, the theoretical predictions are experimentally validated executing an online SBC on a GaN-FET-based higher order high-frequency non-minimum-phase Ćuk-PES. To begin with, time-domain experimental results that validate the offline reachability predictions of the Ćuk-PES, in terms of the frequency, duty cycle, and magnitude of a pulsating load, are conducted by carefully choosing multiple operating points. Next, it is shown experimentally, how the theoretical predictions of the reachability analysis for the Ćuk-PES enable tangible reduction in computation time for online execution of the SBC without any appreciable compromise in system performance and convergence time. Overall, the outlined work has broader ramifications. First, the nonlinear-map-based reachability-analysis approach in terms of a switching sequence of a PES is extendable to other PESs driving pulsating and other type of loads. Second, the reduction in online computation of the SBC, using stability-bound reachable switching sequences, implies that lower cost processor can be used while retaining quality large-signal response expected of optimal controllers.

The SBC approach outlined in this paper is generalizable. A PES is typically designed for CCM, boundary control mode, or discontinuous-conduction mode (DCM). For the first two cases, the methodology outlined in this paper and explained for the specific Ćuk-PES applies as is. If, however, the PES is designed only for DCM, then, the modeling outlined in Section II will simply include an additional switching state corresponding to inductor-current invariance. The reachability analysis remains the same as outlined in Section III with the exception that the search for the time allocation of the switching states of a switching sequence will involve an additional search space to assess the impact of duration inductor current discontinuity or invariance on PES reachability. Optimization methodology in Section IV remains the same with the exception that an additional constraint corresponding to inductor-current invariance needs to be added.

Appendix

The matrices $\hat{A}_{kn}$ and $\hat{B}_{kn}$ for the two switching states of the Ćuk-PES, expressed as $\hat{A}_{kn1}$ and $\hat{B}_{kn1}$ and $\hat{A}_{kn2}$ and $\hat{B}_{kn2}$, respectively, are defined below, where the symbols of the passive components have been defined in Fig. 8

$$\hat{A}_{kn1} = \begin{bmatrix} 0 & 0 & 0 & 0 \\ 0 & 0 & \frac{1}{L_1}\left(2 + \frac{C_1}{2\,C_2}\right) & \frac{-1}{L_2} \\ 0 & \frac{-2}{C_1} & 0 & 0 \\ 0 & \frac{1}{C_{\rm out}} & 0 & -\frac{1}{RC_{\rm out}} \end{bmatrix},$$

$$\hat{B}_{kn1} = \begin{bmatrix} \frac{V_{\rm in}}{L_1} \\ 0 \\ 0 \\ 0 \end{bmatrix}$$

$$\hat{A}_{kn2} = \begin{bmatrix} 0 & 0 & \frac{1}{L_1}\left(-1-\frac{C_1}{4C_2}\right) & 0 \\ 0 & 0 & 0 & \frac{-1}{L_2} \\ \frac{1}{C_1} & 0 & 0 & 0 \\ 0 & \frac{1}{C_{\text{out}}} & 0 & -\frac{1}{RC_{\text{out}}} \end{bmatrix}$$

$$\hat{B}_{kn2} = \begin{bmatrix} \frac{V_{\text{in}}}{L_1} \\ 0 \\ 0 \\ 0 \end{bmatrix}.$$

The pulsating load dynamics are incorporated into the system state-space to form the matrices A_{kn} and B_{kn} for a switching state. The pulsating load dynamics are expressed as harmonic series as in (1). The states of the dynamics of the mth harmonic component can be expressed as follows:

$$y_{m1} = \{a_m \cos(w_m t) + b_m \sin(w_m t)\} \tag{A1}$$

$$\frac{dy_{m1}}{dt} = \{-a_m w_m \sin(w_m t) + b_m w_m \cos(w_m t)\} = y_{m2} \tag{A2}$$

$$\frac{dy_{m2}}{dt} = \{-w_m a_m w_m \cos(w_m t) - w_m b_m w_m \sin(w_m t)\} = -w_m^2 y_{m2}. \tag{A3}$$

Using (A2) and (A3), the states of the harmonic components are combined with $\hat{A}_{kn}$ and $\hat{B}_{kn}$ to form the state-space for the entire system. Matrices A_{kn} and B_{kn} for the two switching states of the system, expressed as A_{kn1} and B_{kn1} and A_{kn2} and B_{kn2}, respectively, have been written below, where m can vary from 1 to ∞

$$A_{kn1} = \begin{bmatrix} \hat{A}_{kn1} & 1 & 0 & . & . & 1 & 0 \\ 0 & 0 & 0 & . & . & 0 & 0 \\ 0 & -w_1^2 & 0 & . & . & 0 & 0 \\ . & . & . & . & . & . & . \\ . & . & . & . & . & . & . \\ 0 & 0 & 0 & . & . & 0 & 1 \\ 0 & 0 & 0 & . & . & -w_\infty^2 & 0 \end{bmatrix}$$

$$B_{kn1} = \begin{bmatrix} \hat{B}_{kn1} + \left(\frac{1}{2}\right) i_{\text{load1}} \\ 0 \\ 0 \\ 0 \\ . \\ . \\ 0 \end{bmatrix}$$

$$A_{kn2} = \begin{bmatrix} \hat{A}_{kn2} & 1 & 0 & . & . & 1 & 0 \\ 0 & 0 & 0 & . & . & 0 & 0 \\ 0 & -w_1^2 & 0 & . & . & 0 & 0 \\ . & . & . & . & . & . & . \\ . & . & . & . & . & . & . \\ 0 & 0 & 0 & . & . & 0 & 1 \\ 0 & 0 & 0 & . & . & -w_\infty^2 & 0 \end{bmatrix}$$

$$B_{kn2} = \begin{bmatrix} \hat{B}_{kn2} + (1/2)\, i_{\text{load1}} \\ 0 \\ 0 \\ 0 \\ . \\ . \\ 0 \end{bmatrix}.$$

The derivation of (8) starting with (7) is delineated in detail as follows:

$$\begin{aligned} \nabla V_k(e) &= \sum_{n=1}^{h} \alpha_{kn} \Big((A_{knd} e(j) + B_{knd})^T \\ &\quad \times P_{kn} (A_{knd} e(j) + B_{knd})) - e(j)^T P_{kn} e(j) \Big) \\ &= \sum_{n=1}^{h} \alpha_{kn} \Big(\Big(e(j)^T A_{knd}^T + B_{knd}^T \Big) \\ &\quad \times P_{kn} (A_{knd} e(j) + B_{knd})) - e(j)^T P_{kn} e(j) \Big) \\ &= \sum_{n=1}^{h} \alpha_{kn} \Big(\Big(e(j)^T A_{knd}^T P_{kn} + B_{knd}^T P_{kn} \Big) \\ &\quad \times (A_{knd} e(j) + B_{knd})) - e(j)^T P_{kn} e(j) \Big) \\ \nabla V_k(e) &= \sum_{n=1}^{h} \alpha_{kn} \Big(e(j)^T A_{knd}^T P_{kn} A_{knd} e(j) \\ &\quad + e(j)^T A_{knd}^T P_{kn}\, B_{knd} + B_{knd}^T P_{kn}\, A_{knd} e(j) \\ &\quad + B_{knd}^T P_{kn}\, B_{knd})) - e(j)^T P_{kn} e(j) \Big) \\ \nabla V_k(e) &= \sum_{n=1}^{h} \alpha_{kn} \Big(e(j)^T (A_{knd}^T P_{kn}\, A_{knd} - P_{kn}) e(j) \\ &\quad + e(j)^T A_{knd}^T P_{kn}\, B_{knd} + B_{knd}^T P_{kn}\, A_{knd} e(j) \\ &\quad + B_{knd}^T P_{kn}\, B_{knd} \Big) \\ \nabla V_k(e) &= \sum_{n=1}^{h} \alpha_{kn} \begin{pmatrix} e(j) \\ 1 \end{pmatrix}^T \\ &\quad \times \begin{bmatrix} (A_{knd}^T P_{kn}\, A_{knd} - P_{kn}) & A_{knd}^T P_{kn}\, B_{knd} \\ B_{knd}^T P_{kn}\, A_{knd} & B_{knd}^T P_{kn}\, B_{knd} \end{bmatrix} \\ &\quad \times \begin{pmatrix} e(j) \\ 1 \end{pmatrix}. \end{aligned} \tag{A4}$$

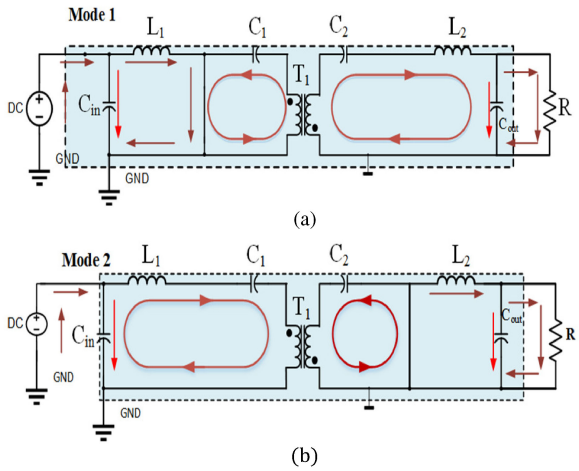

Fig. 20. (a) and (b) Modes of operation of the Ćuk-PES.

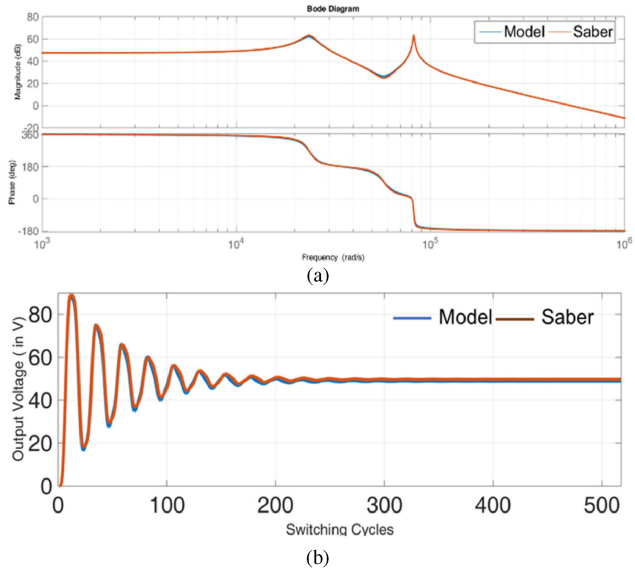

Fig. 21. Comparison of (a) the open-loop Bode plot of $\hat{V}_{\rm out}/\hat{\alpha}_{11}$ and (b) the output voltage predicted by the reduced-order model with that by Saber software simulation.

The modes of operation of the isolated Ćuk converter, which is the PES under consideration (i.e., Ćuk-PES), has been discussed here succinctly. There are primarily two modes of operation, namely modes 1 and 2, which are highlighted next.

Mode 1: In mode 1, the primary switch of the Ćuk-PES is turned ON. The current flowing through the primary side inductor L_1 increases and it stores energy. The capacitor C_1 discharges through the primary side switch resulting in a transfer of energy from the primary to the secondary side of the transformer. The energy stored in the capacitor C_2 is discharged to the circuit formed by L_2, $C_{\rm out}$ and the load R. Fig. 20(a) shows mode 1 of operation.

Mode 2: In mode 1, the primary switch of the Ćuk-PES is turned OFF and the secondary side switch is turned ON. The primary inductor discharges to the primary and secondary blocking capacitors. The output inductor which was charged in mode 1 relinquishes the charge to the output capacitor and the load R. Fig. 20(b) shows mode 2 of operation.

The high-frequency transformer in the Ćuk-PES has a finite leakage of 300 nH referred to the primary side and a magnetizing inductance of 150 μH, which are not incorporated in the prediction model. The leakage inductance is neglected given that it is significantly smaller compared to the series input inductance of the system. To test the efficacy of the reduced-order model used for prediction that does not encompass the magnetizing inductance (L_m), we compare the open-loop Bode plot of the prediction model with that obtained using Saber, which is a powerful system circuit simulator. A detailed simulation model using all the non-idealities, as shown in Fig. 8, is constructed in Saber and the responses are compared. The responses, shown in Fig. 21, almost match one another within the bandwidth of interest, thereby proving the efficacy of the prediction model.

ACKNOWLEDGMENT

This material is supported in part by the U.S. Office of Naval Research (ONR) under Award Nos. N00014-17-1-2695. This material is based in part upon work supported by the U.S. Department of Energy's Office of Energy Efficiency and Renewable Energy (EERE) under Solar Energy Technologies Office (SETO) Agreement Number EE0008349.

REFERENCES

[1] H. W. Gayek and L. R. Peaslee, "Behavior of aircraft generating systems with pulsating loads," *IEEE Trans. Aerosp.*, vol. AS-3, no. 2, pp. 603–614, Jun. 1965.

[2] H. Ebrahimi, H. El-Kishky, M. Biswass, and M. Robinson, "Impact of pulsed power loads on advanced aircraft electric power systems with hybrid APU," in *Proc. IEEE Int. Power Modulator High Voltage Conf.*, 2017, pp. 434–437.

[3] H. Soni, S. K. Mazumder, A. Gupta, D. Chatterjee, and A. Kulkarni, "Control of isolated differential-mode single- and three-phase Ćuk inverters at module level," *IEEE Trans. Power Electron.*, vol. 33, no. 10, pp. 8872–8886, Oct. 2018.

[4] Z. Chen, "PI and sliding mode control of a Ćuk converter," *IEEE Trans. Power Electron.*, vol. 27, no. 8, pp. 3695–3703, Aug. 2012.

[5] S. Guo, X. Lin-Shi, B. Allard, Y. Gao, and Y. Ruan, "Digital sliding-mode controller for high-frequency dc/dc SMPS," *IEEE Trans. Power Electron.*, vol. 25, no. 5, pp. 1120–1123, May 2010.

[6] H. El Fadil and F. Giri, "Backstepping based control of pwm dc-dc boost power converters," in *Proc. IEEE Int. Symp. Ind. Electron.*, 2007, pp. 395–400.

[7] H. Rodr, R. Ortega, and A. Astolfi, "Adaptive partial state feedback control of of the dc-to-dc Ćuk converter," in *Proc. IEEE Amer. Control Conf.*, Jun. 2005, pp. 5121–5126.

[8] H. Sira-Ramirez and M. T. Prada-Rizzo, "Nonlinear feedback regulator design for the Cuk converter," *IEEE Trans. Automat. Control*, vol. 37, no. 8, pp. 1173–1180, Aug. 1992.

[9] S. K. Mazumder and K. Acharya, "Multiple Lyapunov function based reaching condition for orbital existence of switching power converters," *IEEE Trans. Power Electron.*, vol. 23, no. 3, pp. 1449–1471, May 2008.

[10] A. Tajfar and S. K. Mazumder, "Sequence-based control of an isolated dc/ac matrix converter," *IEEE Trans. Power Electron.*, vol. 31, no. 2, pp. 1757–1773, Feb. 2016.

[11] T. Geyer, "Computationally efficient model predictive direct torque control," *IEEE Trans. Power Electron.*, vol. 26, no. 10, pp. 2804–2816, Oct. 2011.

[12] J. Rodriguez, P. Cortes, R. Kennel, and M. Kazrnierkowski, "Model predictive control – A simple and powerful method to control power converters," in *Proc. IEEE 6th Int. Power Electron. Motion Control Conf.*, 2009, pp. 41–49.

[13] S. Mariéthoz and M. Morari, "Explicit model-predictive control of a PWM inverter with an LCL filter," *IEEE Trans. Ind. Electron.*, vol. 56, no. 2, pp. 389–399, Feb. 2009.

[14] M. Votava, V. Smidl, T. Glasberger, and Z. Peroutka, "Model predictive control of dual inverter respecting temperature limits of IGBTs," in *Proc. 18th Eur. Conf. Power Electron. Appl.*, 2016, pp. 1–10.
[15] R. Vargas, U. Ammann, and J. Rodríguez, "Predictive approach to increase efficiency and reduce switching losses on matrix converters," *IEEE Trans. Power Electron.*,vol. 24, no. 4, pp. 894–902, Apr. 2009.
[16] L. Cheng *et al.*, "Model predictive control for dc-dc boost converters with reduced-prediction horizon and constant switching frequency," *IEEE Trans. Power Electron.*, vol. 33, no. 10, pp. 9064–9075, Oct. 2018.
[17] R. P. Aguilera *et al.*, "Selective harmonic elimination model predictive control for multilevel power converters," *IEEE Trans. Power Electron.*, vol. 32, no. 3, pp. 2416–2426, Mar. 2017.
[18] D. Limon, A. Ferramosca, I. Alvarado, and T. Alamo, "Nonlinear MPC for tracking piece-wise constant reference signals," *IEEE Trans. Automat. Control*, vol. 63, no. 11, pp. 3735–3750, Nov. 2018.
[19] T. Geyer, G. Papafotiou, and M. Morari, "Model predictive direct torque control—Part I: Concept, algorithm, and analysis," *IEEE Trans. Ind. Electron.*, vol. 56, no. 6, pp. 1894–1905, Jun. 2009.
[20] P. Karamanakos, T. Geyer, and S. Manias, "Direct model predictive current control strategy of dc-dc boost converters," *IEEE J. Emerg. Sel. Topics Power Electron.*, vol. 1, no. 4, pp. 337–346, Dec. 2013.
[21] P. Karamanakos, T. Geyer, and S. Manias, "Direct voltage control of dc-dc boost converters using enumeration-based model predictive control," *IEEE Trans. Power Electron.*, vol. 29, no. 2, pp. 968–978, Feb. 2014.
[22] P. Karamanakos, T. Geyer, and S. Manias, "Direct model predictive current control of dc-dc boost converters," in *Proc. 15th Int. Power Electron. Motion Control Conf.*, 2012, pp. DS2c.11-1–DS2c.11-8.
[23] J. Neely, R. DeCa, and S. Pekarek, "Real-time model predictive control of the Ćuk converter," in *Proc. IEEE 12th Workshop Control Model. Power Electron.*, 2010, pp. 1–8.
[24] F. M. Oettmeier, J. Neely, S. Pekarek, R. DeCarlo, and K. Uthaichana, "MPC of switching in a boost converter using a hybrid state model with a sliding mode observer," *IEEE Trans. Ind. Electron.*, vol. 56, no. 9, pp. 3453–3466, Sep. 2009.
[25] V. Grigore, J. Hatonen, J. Kyyra, and T. Suntio, "Dynamics of a buck converter with a constant power load," in *Proc. 29th Annu. IEEE Power Electron. Spec. Conf.*, 1998, vol. 1, pp. 72–78.
[26] A. Emadi, A. Khaligh, C. H. Rivetta, and G. A. Williamson, "Constant power loads and negative impedance instability in automotives systems: Definition, modeling, stability, and control of power electronic converters and motor drives," *IEEE Trans. Veh. Technol.*, vol. 55, no. 4, pp. 1112–1125, Jul. 2006.
[27] I. Kondratiev, E. Santi, R. Dougal, and G. Veselov, "Synergetic control for dc/dc buck converters with constant power load," in *Proc. IEEE 35th Annu. Power Electron. Spec. Conf.*, 2004, pp. 3758–3764.
[28] M. M. Jovanovic, C. S. Leu, and F. C. Y. Lee, "Zero-voltage-switched multiresonant converter for high-power, pulse-load applications," *IEEE Trans. Ind. Electron.*, vol. 37, no. 6, pp. 544–555, Dec. 1990.
[29] J. M. Crider and S. D. Sudhoff, "Reducing impact of pulsed power loads on microgrid power systems," *IEEE Trans. Smart Grid*, vol. 1, no. 3, pp. 270–277, Dec. 2010.
[30] P. Alou, J. A. Cobos, O. Garcia, R. Prieto, and J. Uceda, "Coupling inductors for supplying pulsating loads with dc-dc converters," in *Proc. 29th Annu. IEEE Power Electron. Spec. Conf.*, 1998, vol. 2, pp. 1790–1795.
[31] N. Vishwanathan and V. Ramanarayanan, "High voltage dc power supply topology for pulsed load applications with converter switching synchronized to load pulses," in *Proc. Int. Conf. Power Electron. Drive Syst.*, 2003, vol. 1, pp. 618–623.
[32] J. T. Broach, "Converters for supplying pulsed power loads," *IEEE Trans. Ind. Appl.*, vol. IA-15, no. 1, pp. 85–91, Jan. 1979.
[33] X. Huang, X. Ruan, F. Du, F. Liu, and L. Zhang, "High power and low voltage power supply for low frequency pulsed load," in *Proc. IEEE Appl. Power Electron. Conf. Expo.*, 2017, pp. 2859–2865.
[34] X. Huang, X. Ruan, F. Du, F. Liu, and L. Zhang, "A pulsed power supply adopting active capacitor converter for low-voltage and low-frequency pulsed loads," *IEEE Trans. Power Electron.*, vol. 33, no. 11, pp. 9219–9230, Nov. 2018.
[35] Q. Yang, L. Tan, W. Liu, and W. Im, "Adaptive critic design based cooperative control for pulsed power loads accommodation in shipboard power system," *IET Gener. Transmiss. Distrib.*, vol. 10, no. 11, pp. 2739–2747, 2016.
[36] M. M. Mardani, M. H. Khooban, A. Masoudian, and T. Dragicevic, "Model predictive control of dc-dc converters to mitigate the effects of pulsed power loads in naval dc microgrids," *IEEE Trans. Ind. Electron.*, vol. 66, no. 7, pp. 5676–5685, Jul. 2019.
[37] G. Tan, B. Kou, H. Wu, and L. Li, "Dynamic sensorless detection of linear electromagnetic UAV launch," *IEEE Trans. Plasma Sci.*, vol. 39, no. 1, pp. 399–404, Jan. 2011.
[38] Y. Komaru, Y. Inoue, S. Morimoto, and M. Sanada, "Comparative study of speed ripple reduction by various control methods in pmsm drive systems with pulsating load," in *Proc. Int. Power Electron. Conf.*, 2018, pp. 1329–1335.
[39] R. Cao, Y. Jin, M. Lu, and Z. Zhang, "Quantitative comparison of linear flux-switching permanent magnet motor with linear induction motor for electromagnetic launch system," *IEEE Trans. Ind. Electron.*, vol. 65, no. 9, pp. 7569–7578, Sep. 2018.
[40] R. Redl and N. O. Sokal, "Near-optimum dynamic regulation of dc-dc converters using feed-forward of output current and input voltage with current-mode control," *IEEE Trans. Power Electron.*, vol. PE-1, no. 3, pp. 181–192, Jul. 1986.
[41] A. G. Beccuti, G. Papafotiou, and M. Morari, "Optimal control of the boost dc-dc converter," in *Proc. 44th IEEE Conf. Dec. Control*, 2005, pp. 4457–4462.
[42] P. Cortes *et al.*, "Guidelines for weighting factors design in model predictive control of power converters and drives," in *Proc. IEEE Int. Conf. Ind. Technol.*, 2009, pp. 1–7.
[43] A. Kulkarni, A. Gupta, and S. K. Mazumder, "Resolving practical design issues in a single-phase grid-connected GaN-FET-based differential-mode inverter," *IEEE Trans. Power Electron.*, vol. 33, no. 5, pp. 3734–3751, May 2018.

Debanjan Chatterjee (S'19) received the B.E. degree in electrical engineering from Jadavpur University, Kolkata, India, in 2015. He is currently working toward the Ph.D. degree in electrical and computer engineering at The University of Illinois at Chicago, Chicago, IL, USA.

His research interests include digital control and modulation of power electronic converters. He is currently working in model predictive, switching sequence, and switching transition controllers for GaN-based power electronic systems.

Sudip Kumar Mazumder (S'97–M'01–SM'03–F'16) received the M.S. degree in electrical power engineering from Rensselaer Polytechnic Institute, Troy, NY, USA, in 1993, and the Ph.D. degree in electrical and computer engineering from Virginia Tech, Blacksburg, VA, USA, in 2001.

He has been a Professor with the University of Illinois at Chicago, Chicago, IL, USA, since 2001, and is the President of Next Watt LLC since 2008. He has more than 25 years of professional experience and has held R&D and design positions in leading industrial organizations and has served as a Technical Consultant for several industries. He has published more than 200 refereed papers, delivered over 85 keynote/plenary/invited presentations, and received and carried out about 50 sponsored research since joining UIC.

Dr. Mazumder is the recipient of the UICs Inventor of the Year Award (2014), the University of Illinois University Scholar of the Year Award (2014), the University of Illinois University Scholar Award (2013), the Office of Naval research Young Investigator Award (2005), the National Science Foundation CAREER Award (2003), and the IEEE Power Electronics Society (PELS) Transaction Paper Award (2002). He has served on several prestigious National Science Foundation panels. In 2016, he was elevated to the rank of an IEEE Fellow and was elected to serve as a Distinguished Lecturer for IEEE PELS beginning in 2016. He has served/is serving as the Guest Editor-in-Chief/Editor for IEEE PELS/IES Transactions between 2013 and 2017, as the first Editor-in-Chief for *Advances in Power Electronics* (2006–2009), and as an Editorial Board Member for IEEE TPEL/TIE/TII/JESTPE/TAES transactions. He currently serves as the Chair for IEEE PELS Technical Committee on Sustainable Energy Systems and as an AdCom Member for PELS. He is also involved with several of IEEE, PELS, and PES initiatives including International Technology Roadmap for Wide-Bandgap (ITRW) Technologies, Billion Smiles, Smart Village, and Microgrid Task Force.